Original Article

Institution of MECHANICAL ENGINEERS
Journal of MECHANICAL ENGINEERING SCIENCE

Numerical simulation and experimental study of the air-cooled motorized spindle

Proc IMechE Part C:
J Mechanical Engineering Science
2017, Vol. 231(12) 2357–2369

DOI: 10.1177/0954406216631781
journals.sagepub.com/home/pic
SAGE

He Qiang[1], Shen Yuan[1], Ren Fengzhang[2], Li Lili[1] and A Volinsky Alex[3]

Abstract

In this study, numerical methods are used to investigate the flow and temperature fields of the air-cooled motorized spindle. The wind speed effects on the motorized spindle temperature and the relationships between the rotating speed, vibration and noise are studied experimentally. The purpose of this work is to provide the basis for optimization design of the air-cooled motorized spindle. First, the boundary conditions are defined and the wind speed in the heat sink groove, fluid field of the fan area and temperature distribution of the spindle in the thermal steady state are predicted by the finite element method. Second, the temperature, wind speed, vibration of the key points on the motorized spindle and the noise are measured experimentally. The results show that the wind speed of the fan area is high in the center and low near the wall. The spindle temperature is higher in the area of contact with the rotor and the front bearings, while changes in the heat sink section have little effect on the wind speed. It is found experimentally that the vibration, noise and temperature increase with rotating speed. The numerical and experimental results are consistent. It is suggested to improve the design of the motorized spindle through optimizing the blade structure to decrease the temperature, vibration and noise.

Keywords

Air-cooled motorized spindle, temperature distribution, vibration, noise, fluid flow

Date received: 30 November 2014; accepted: 12 November 2015

Introduction

The motorized spindle plays a vital role in improving the machining precision and processing efficiency of the manufactured goods. Among all errors that affect the motorized spindle precision, thermal errors cause most problems.[1] Wood needs to be protected from water and oil during the machining process. Typically, cooling of the motorized spindle in wood-working is achieved by means of an axial fan, where a fan blade is installed at the rear of the spindle to blow cooling air. For the wood-working motorized spindle with the air-cooling system, its vibration and noise character, impacted by the wind, will be different from the traditional motorized spindle.

Previous experiments and numerical simulations of the fluid machinery often focus on studying the blade to improve its performance.[2–4] Mori et al.[5] studied an axial flow fan operating under rotating stall conditions using particle image velocimetry method and numerical analysis. Sadowski and Golewski[6] compared thermal characteristics of the turbine blade with applied thermal barrier coatings and the normal turbine blade. Fike et al.[7] introduced a visualization system of the axial flow fan and studied the flow distribution around the blade. Allison et al.[8] discussed the air-cooled heat exchanger with interdigitated impeller blades and provided a design method for the heat exchanger. Zhao et al.[9] studied the thermal behavior of the CNC machine tool spindle using the finite element method and showed good agreement with experimental results. Holkup et al.[10] presented a thermo-mechanical model of the spindle that can simulate the bearing performance and thermo-mechanical deformation of the spindle parts. Anandan and Ozdoganlar[11] found that the thermal

[1]Department of Mechanical Engineering, Anyang Institute of Technology, Anyang, China
[2]School of Materials Science and Engineering, Henan University of Science and Technology, Luoyang, China
[3]Department of Mechanical Engineering, University of South Florida, Tampa, FL, USA

Corresponding author:
Ren Fengzhang, School of Materials Science and Engineering, Henan University of Science and Technology, Luoyang, China.
Email: aystar@163.com

character, rotating speed of the spindle and span all have impact the performance of the ultrahigh-speed micromachining spindle. Zahedi and Movahhedy[12] studied the relations between generated heat, stiffness, rotating speed and natural frequency. However, only a few researchers have studied the dynamic characteristics and the fluid flow of the air-cooled motorized spindle.

This paper studied the fluid flow and the temperature distribution of the air-cooled motorized spindle. The wind speed effects the motorized spindle temperature and the relationships between the rotating speed, vibration and noise were studied experimentally. In this paper, the fluid flow was investigated by the finite element method, and a thermal model was built to simulate the thermal characteristics of the spindle. Numerical results are verified by experiments which are consistent with the experimental results.

Numerical model

The problem is complicated because the heat transfer in the motorized spindle involves both internal and external heat exchange. However, it is difficult to study the internal heat exchange character without breaking the overall structure of the motorized spindle. A better solution at present is to simulate the heat and fluid flow using numerical methods.

The Navier-Stokes equations express the Newton's second law for the motion–force and acceleration of the incompressible viscous flow. They represent the fundamental mathematical model of fluid dynamics problems.[13] These equations include the conservation of mass or continuity equation, the conservation of momentum equation and the conservation of energy equation.

The conservation of mass equation using an indicial notation is

$$\frac{\partial u_i}{\partial x_i} = 0 \tag{1}$$

where $i = 1, 2$ for the two-dimensional case and $i = 1, 2, 3$ for the three-dimensional flow.

The conservation of momentum equation is

$$\rho\left(\frac{\partial u_i}{\partial t} + u_j\frac{\partial u_i}{\partial x_j}\right) = -\frac{\partial p}{\partial x_i} + \mu\left(\frac{\partial^2 u_i}{\partial x_i^2}\right) \tag{2}$$

This equation is applicable in any space dimensions.

The energy conservation equation in the indicial form is

$$\frac{\partial T}{\partial t} + u_i\frac{\partial T}{\partial x_i} = \alpha\frac{\partial^2 T}{\partial x_i^2} \tag{3}$$

This equation is applicable in any space dimensions.

The k-ε turbulence model fits most engineering turbulence conditions quite well; it is a two-equation model that solves for the speed and length separately. The k is the turbulent kinetic energy, which stands for the variation of velocity fluctuations. The ε is the dissipation rate of the turbulent kinetic energy, which stands for the dissipation rate of the velocity fluctuations.

The standard k-ε turbulence model is

$$\rho\frac{dk}{dt} = \frac{\partial}{\partial x_i}\left[\left(\mu + \frac{\mu_i}{\sigma_k}\right)\frac{\partial k}{\partial x_i}\right] + G_k + G_b - \rho\varepsilon - Y_M \tag{4}$$

$$\rho\frac{\mathrm{d}\varepsilon}{dt} = \frac{\partial}{\partial x_i}\left[\left(\mu + \frac{\mu_i}{\sigma_\varepsilon}\right)\frac{\partial \varepsilon}{\partial x_i}\right] + C_{\varepsilon_1}\frac{\varepsilon}{k}\left(G_k + C_{\varepsilon_3}G_b\right) - C_{\varepsilon_2}\rho\frac{\varepsilon^2}{k} \tag{5}$$

where C_{ε_1}, C_{ε_2}, C_{ε_3}, σ_k, σ_ε are constant[14] ($C_{\varepsilon_1} = 1.44$, $C_{\varepsilon_2} = 1.92$, $C_{\varepsilon_3} = 0.09$, $\sigma_k = 1.0$, $\sigma_\varepsilon = 1.3$). G_k stands for the turbulent kinetic energy generated by the average velocity gradient. G_b stands for the turbulent kinetic energy generated by buoyancy. Y_M stands for the influence of compressible turbulent flow pulsation on the total dissipation rate. The turbulent viscosity coefficient, μ_i, can be expressed as

$$\mu_i = \rho C_\mu\frac{\varepsilon^2}{k} \tag{6}$$

Fluid flow boundary conditions. It is very important to know the heat dissipating capacity of the fan and the sink when designing the air-cooled motorized spindle. The heat dissipating capacity of the sink at a certain mass flow is the key concern of this paper. In this case, the flowing fluid is air with velocity-inlet boundary conditions of the fan vents, while the temperature of the fluid is the same as the room temperature. Turbulent kinetic energy is 0.5% of the average kinetic energy of the inflowing fluid. Hydraulic diameter uses the characteristic length of the heat sink around the air inlets. The boundary conditions of the fluid outlet are defined by the outlet pressure.

Heat generation in the bearings and the motor

Heat generation in the bearings:

Palmgren[15] gives empirical formulas for calculating the heat generated in the bearings

$$Q_f = 1.047 \times 10^{-4} M \cdot n \tag{7}$$

where M is the total friction torque of the bearings ($N{\cdot}mm$), n is the rotating speed of the bearing inner race (r/min) and Q_f is the heat generated in the bearings (W).

The total friction torque of the bearings consists of the two terms

$$M = M_1 + M_2 \tag{8}$$

M_1 is the friction torque related to the rotating speed, lubrication and bearing type, and can be calculated as

$$M_1 = 10^{-7} \times f_0 (vn)^{2/3} d_m^3 \quad vn > 2000 \tag{9}$$

$$M_1 = 160 \times 10^{-7} f_0 d_m^3 \quad vn < 2000 \tag{10}$$

where f_0 is a coefficient related to the bearing type and lubrication. For the angular contact ball bearings lubricated by grease, $f_0 = 2$; d_m is the mid-diameter of the bearings; v is the kinematic viscosity of the lubricant at operating temperature. For the ball bearings lubricated by grease, it means that the base oil kinematic viscosity of grease is valid for a short period after greasing.[16]

M_2 is the friction torque related to the load of the bearing. It can be calculated as

$$M_2 = f_1 P_1 d_m \tag{11}$$

where f_1 is the load coefficient, and for the angular contact ball bearings $f_1 = 0.001$; P_1 is the equivalent load of the bearings.

Heat generation in the motor:

Copper loss is the electric energy loss caused by the resistance of the rotor and the stator winding, given by[17]

$$P_{cm} = \theta I_p^2 r = \frac{\theta I_p^2 \rho_p L_p}{S} \tag{12}$$

where θ is the number of phases of the motor, I_p is the phase current of the rotor or stator winding (A), r is the resistance of the single-phase rotor or stator winding (Ω), ρ_p is the resistivity of the winding ($\Omega \cdot m$), L_p is the length of each phase winding (m), S is the cross-sectional area of the conductor (m^2).

Iron loss (magnetic loss) is another loss of the motor, which can be calculated as[17]

$$P_{Fe} = P_{1/50} \left(\frac{f}{50} \right)^{4/3} k_a B^2 m_c \tag{13}$$

where $P_{1/50}$ is the iron loss coefficient when $B = 1\,T$ and $f = 50\,\text{Hz}$, m_c is the mass (kg), B is the magnetic flux (T).

Heat transfer coefficients. The flow state of the air in the heat sink can be described by the Reynolds number (Re). The cross-section of the heat sink is U-shaped cross-section and its hydraulic radius can be used as the characteristic length

$$R = A/x \tag{14}$$

$$\text{Re} = \frac{\bar{v}}{\nu} R \tag{15}$$

where A is the cross-sectional area, x is the wetted perimeter of the cross-section, $\bar{v}$ is the mean flow velocity of the fluid, ν is the kinematic viscosity of the fluid.

When $\text{Re} < 2200$ the flow state is laminar flow, and the Nusselt number is given by[18]

$$Nu_f = 0.46 Re_f^{0.5} Pr_f^{0.43} \left(\frac{Pr_f}{Pr_w} \right)^{0.25} \left(\frac{d}{L} \right)^{0.4} \tag{16}$$

where L is the length of the heat sink, d is the characteristic length of the flow pass diameter ($d = 4R$), Pr_w is calculated according to the wall temperature, T_w. The experimental verification scope: $1.41 < Pr_f / Pr_w < 18.2$, $Re_f < 2200$.

For $2200 < \text{Re} < 10{,}000$, the average heat transfer coefficients of air is given by[18]

$$Nu_f = 0.0214 \left(Re_f^{0.8} - 100 \right) \times Pr_f^{0.4} \left[1 + \left(\frac{d}{L} \right)^{2/3} \right] \left(\frac{T_f}{T_w} \right)^{045} \tag{17}$$

The temperature, T_f, is the average value of the inlet and the outlet fluid temperature. The experimental verification scope: $0.6 < Pr_f < 1.5$, $0.5 < \text{T}_f/\text{T}_w < 1.5$, $2200 < Re_f < 10{,}000$.

When the flow state is strongly turbulent ($\text{Re} > 10{,}000$), the Nusselt number is typically calculated by the Dittus-Boelter formula[18]

$$Nu_f = 0.023 \text{Re}_f^{0.8} Pr_f^{\text{n}} \tag{18}$$

$\text{n} = 0.4$ when cooling the fluid and $\text{n} = 0.3$ when heating the fluid. This formula is suitable for the condition when the temperature difference is below the medium (no more than 50°C for gas). The experimental verification scope: $10{,}000 < Re_f < 120{,}000$, $0.7 < Pr_f < 120$, $L/d > 60$.

The Nusselt number of the front heat sink wind area is given by[18]

$$Nu_f = 0.664 \text{Re}_f^{0.5} Pr_f^{1/3} \tag{19}$$

The heat transfer coefficients of the forced convection is given by

$$h_w = \frac{Nu \lambda_w}{d} \tag{20}$$

where Nu is the Nusselt number of the fluid that can be calculated using the above equations, and λ_w is the thermal conductivity of the fluid.

The heat exchange is complicated in the air gap between the rotor and the stator, and the simplified heat transfer coefficients can be given by[19]

$$h_g = 28 \left(1 + \omega_\sigma^{0.5} \right) \tag{21}$$

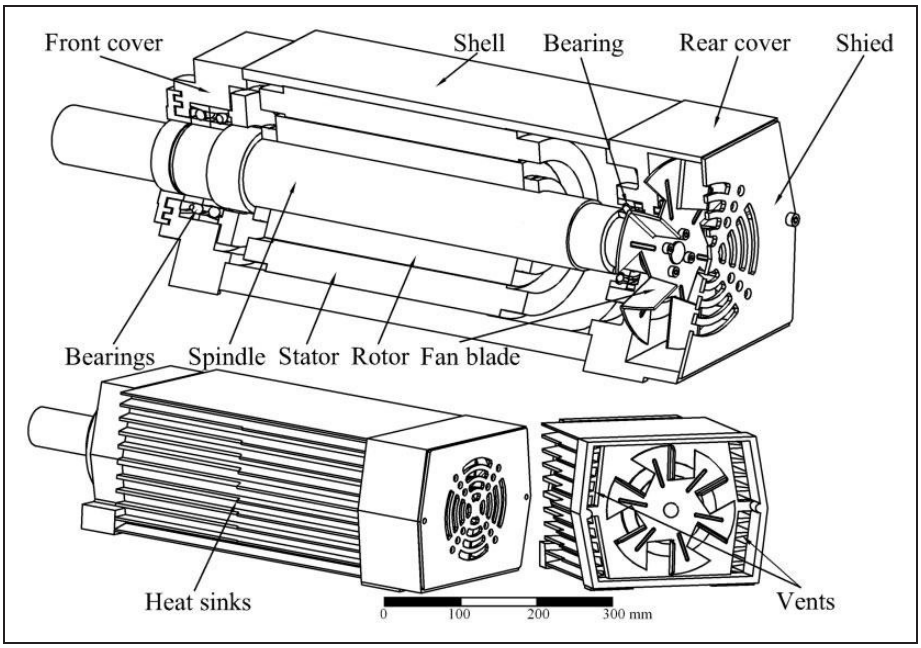

Figure 1. The structure of the motorized spindle.

where ω_σ is the average wind velocity of the gap ($\omega_\sigma = v_a/2$), v_a is rotating speed of the rotor).

The simplified heat transfer coefficients of the spindle surface can be given by[19]

$$h_t = 28\left(1 + \sqrt{0.45 v_t}\right) \tag{22}$$

where v_t is the velocity of the spindle surface, as for the end region of the rotor and the spindle, v_t is the average velocity of their end region.

The heat transfer of the motorized spindle surface includes convection and radiation. The entire thermal resistance can be seen as parallel two thermal resistances, so the entire heat transfer equals the sum of the convection and radiation heat transfer

$$\Phi = \Phi_c + \Phi_R \tag{23}$$

where Φ is the entire heat transfer, Φ_c is the convection heat transfer, Φ_R is the radiation heat transfer. According to Chen and Chen,[20] the heat transfer coefficient of the motorized spindle surface is 31.6 W/($m^{2\circ}$C).

Figure 1 shows an air-cooled motorized spindle, whose power is 8 KW, while the operating voltage is 380 V, and the rotating speed is 6000 r/min. The spindle is supported by the front and the rear bearings. The front bearings are two angular contact ball bearings (7010C/P4) and adopt the face-to-face mounting. The rear bearing is a deep-groove ball bearing (6007) and is compressed by a wave spring. The wave spring can compensate the thermal deformation of the spindle. The lubricating grease is Kluber L252. The spindle cooling fan is a stamped product with six fan blades mounted on the spindle by four hexagonal head bolts. Outside the fan area, a shield was mounted for protection. There are four vents in the rear cover to let the cold air pass.

The numerical model is simplified according to the real motorized spindle. The model can be divided into the fluid analysis model and the heat transfer model.

Different computational domains have different parameter settings in fluid analysis. As shown in the Figure 2, the fluid analysis model is divided into two parts, one is the rotating domain around the fan area and another is the fixed domain, which is the rest of the fluid area. The rotating domain includes the cylinder that envelopes the fan and the interface between air and the fan. The rest of the fluid area is a fixed part for the fluid state calculations.

It is important to simplify the model for the thermal analysis. In the simulation of the motorized spindle, the rotor and the stator can be simplified as thick cylinders with evenly distributed heat source. The rolling elements of the bearing can be equivalent to a ring with the same cross-sectional area. The simplified heat source of the bearings is an evenly distributed heat source and the heat flows out through the external surface and the area in contact with the bearing housing. The wiring structure, the bolts, bolt holes and other tiny structures are neglected. The thermal contact resistance of the contact parts in the simplified model is 0. The simplified model is shown in Figure 3.

The bearings and motor heat generation rate and the heat transfer coefficient of all the surfaces can be calculated as in the Heat generation in the bearings and the motor section. In addition, it should be noted that the cross-section of the heat sink changes in the middle, the front surface of the heat sink is about a quarter less than the latter half. Thus, the heat sink characteristic length was used for numerical

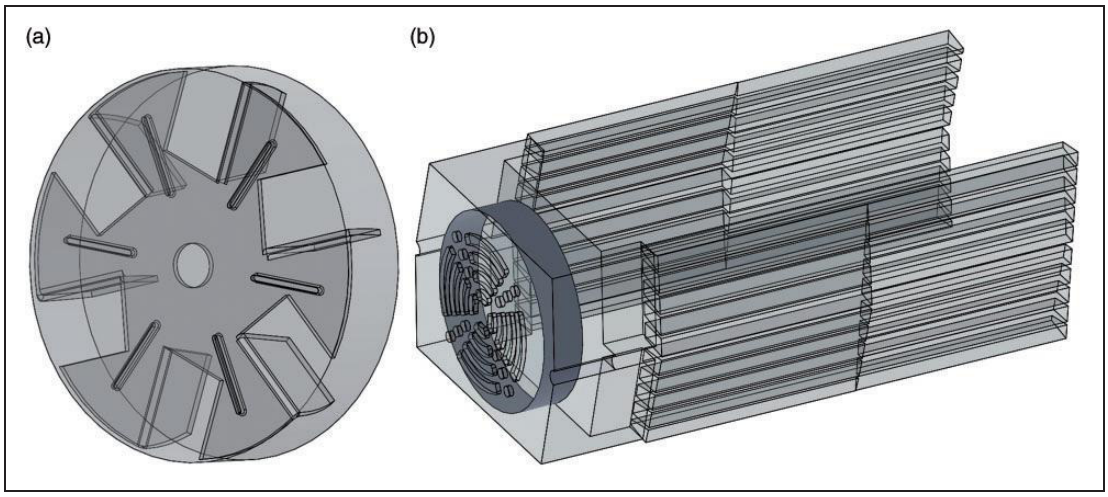

Figure 2. Physical model of the fluid: (a) the rotating domain and (b) the fixed domain.

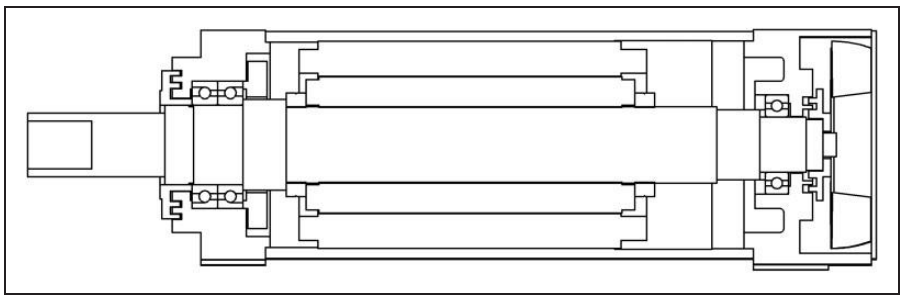

Figure 3. The simplified model of the motorized spindle.

calculations of the latter half of the heat sink, while the wind speed in the heat sink grooves was adopted as three quarters of the mean wind speed value.

Numerical results

The numerical simulation utilized the above numerical model. To obtain the wind speed of the fan area, the ANSYS CFX 14.5 commercial code was applied. The environment temperature of the simulation is 27°C, the rotating speed is 6000 r/min and the influence of natural wind is neglected in the fluid field simulations.

Figure 4 shows the numerical results of the velocity streamline in the fan area. It shows a vortex in the upper-left corner of the fan area. The cooling air enters the fan area from the shield and flows with the fan (the fan rotating direction is counterclockwise). Some air flows out from the vents, while some hits the shield and flows together with the newly entered cooling air, which is why there is a vortex in the upper-left corner. This is because the vortex interacts with the fan and the wind speed (about 70 m/s) is higher than in all other areas. The wind speed is around 10 to 45 m/s in most areas of the fan. The wind speed is higher in the center and lower close to the wall.

The internal temperature of the motorized spindle is shown in Figure 5, which was performed with the commercial code ANSYS Workbench. Among all heat sources (front and rear bearings and the motor) of the motorized spindle, the temperature of the front bearings and the rotor is higher, so the spindle temperature of the contact areas is also higher. The end of the spindle is close to the fan and has good heat dissipation, so is the rear bearings.

Experimental study of the motorized spindle

It is important to consider many factors when choosing the experimental setup facilities. The purpose of the experiments is to investigate the wind speed effects on the motorized spindle temperature and the relationships between the rotating speed, vibration and noise. Thus, the main parameters are related to the fluid and the temperature of the motorized spindle, like wind speed, wind temperature, air density, the rotating speed, vibration, noise and the temperature of the motorized spindle. The fin pitch of the heat sink is less than 15 mm, so the Smart Sensor AR866 hot-film anemometer is chosen to measure the wind speed and air temperature. The surface temperature of the motorized spindle is measured by the infrared thermometer (Shaanxi RG Automatic Instrument

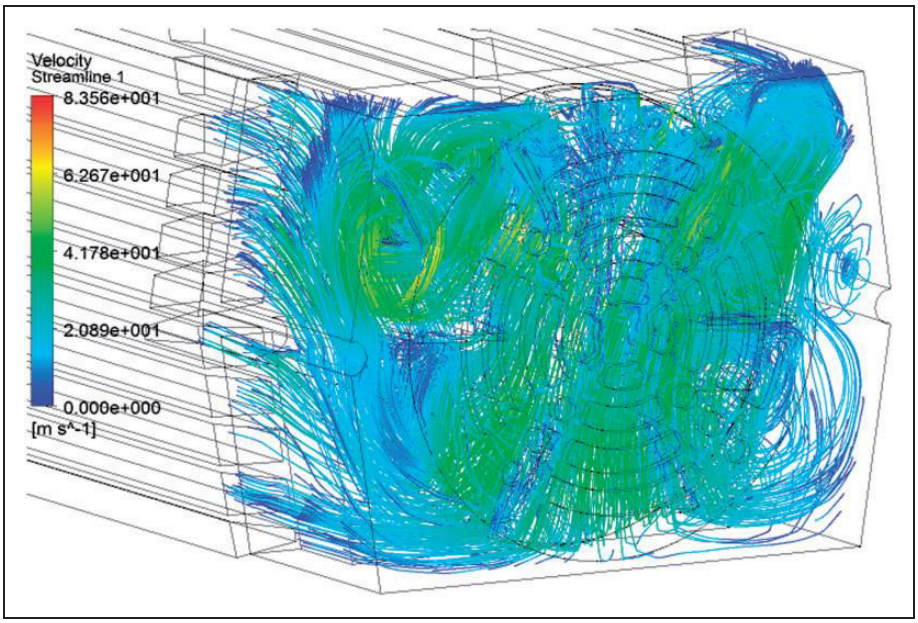

Figure 4. Velocity streamline of the fan area.

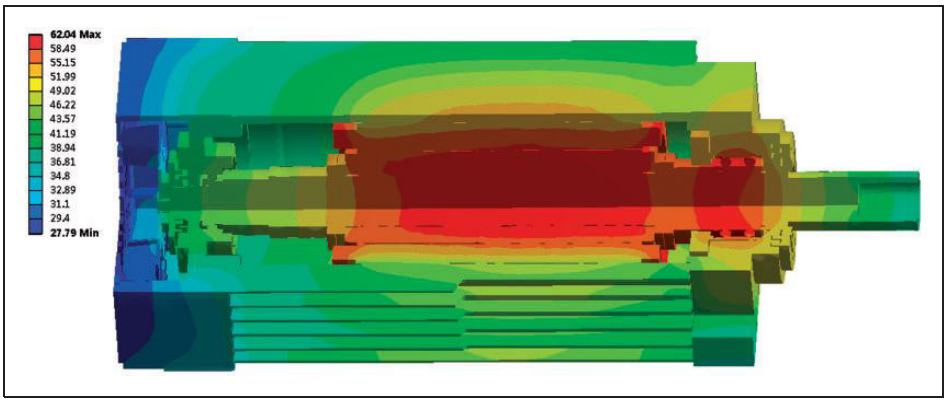

Figure 5. Temperature distribution of the motorized spindle.

PT120). The rotating speed and the vibration are measured by the overall dynamic balance instrument (wiBalancer). The noise is measured by the digital sound level meter (CEM DT-8852).

Figure 6 shows the experimental setup. The ambient temperature is 27°C and the temperature of the entire motorized spindle surface is assumed to be the same. The natural air flow in the lab is less than 0.1 m/s. In order to make sure the rotating speed exactly meets the test requirements, the speed sensor is set at the front of the spindle to measure the rotating speed.

Figure 7(a) shows the map of the surface sampling points. There are nine lines of the sampling points and each line has 30 sampling points, with the 270 sampling points in total. As shown in the Figure 7(c), there are nine sampling point lines along the Y direction dividing the motorized spindle into nine sampling planes, and each plane is divided evenly by the 30 points (30 sampling points along the X direction). Among all the points, there are five key sampling points (points 1 (15,1), 2 (15,5), 3 (15,9), 4 (25,5), and point 5 (5,5)). In the temperature rise experiments, the temperature of the key points is recorded each minute. In the experiment of the steady-state temperature, the temperature of every sampling point is also recorded. In the wind speed experiment under the condition of steady-state temperature, the wind speed of the heat sink groove at each sampling point is recorded. In addition, there is a vibration sampling point in the front bearing area. All reported experimental data have the mean value of five experiments.

Temperature characteristics of the motorized spindle. Figure 8 shows the temperature rise of the motorized spindle at the normal operating rotating speed (6000 r/min). Figure 8(a) shows the temperature comparison of the first three key sampling points, which are all in the $Y = 5$ sampling plane. The temperature is almost the same on the same sampling plane. The

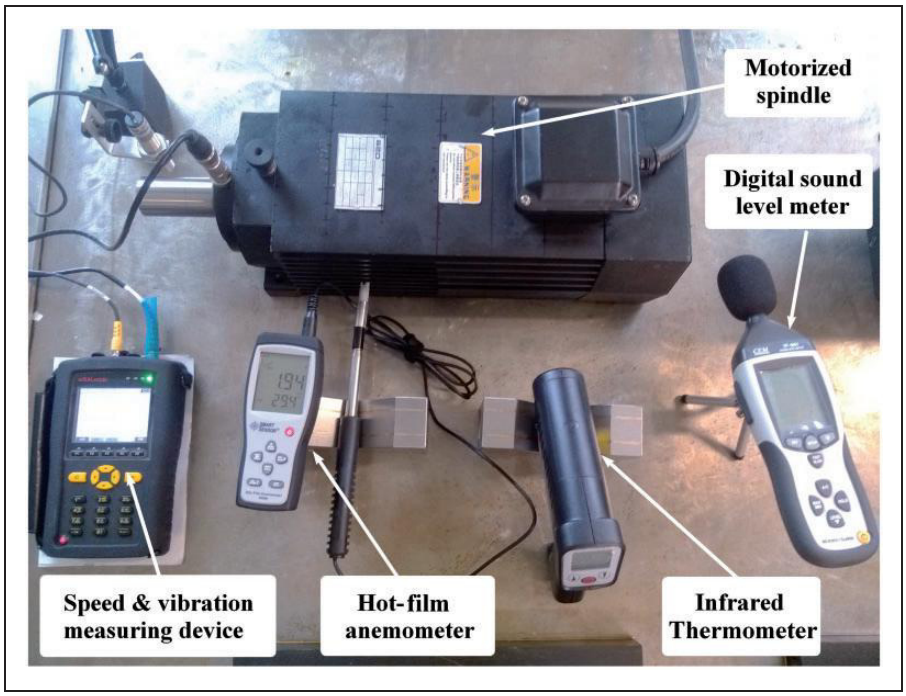

Figure 6. Experimental setup.

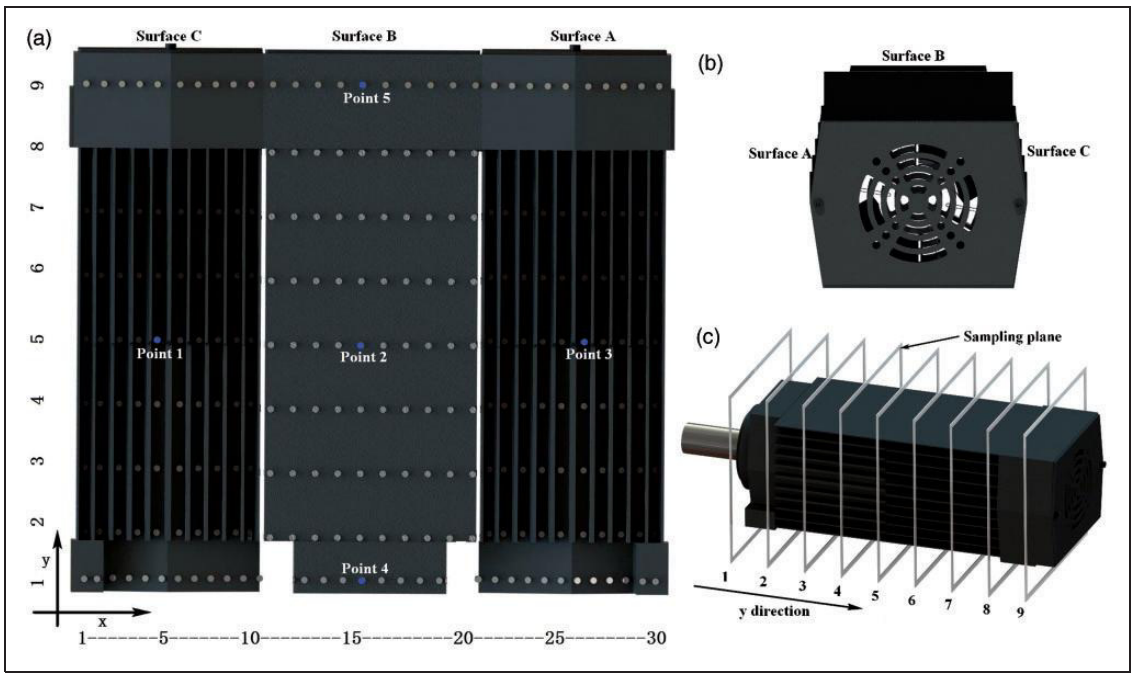

Figure 7. Schematics of the sampling points: (a) surface development figure; (b) back view of the motorized spindle; (c) sketch of the sampling planes.

temperature rise of the sampling point 2 on the surface B is a little faster than the other two sampling points, since there is no wind blowing through the surface B. The temperature rise trend of a sampling plane has only a slight difference, so the temperature trend of the whole motorized spindle can be represented by the front, middle and rear points (points 4, 2, 5). As shown in Figure 8(b), the front side of the motorized spindle reaches the steady thermal state first. In addition, the temperature of the front is a little lower than the middle in the first 25 min and higher after that. This is because there is not only bearings heat in the front of the motorized spindle but also the cooling air is heated at the latter part,

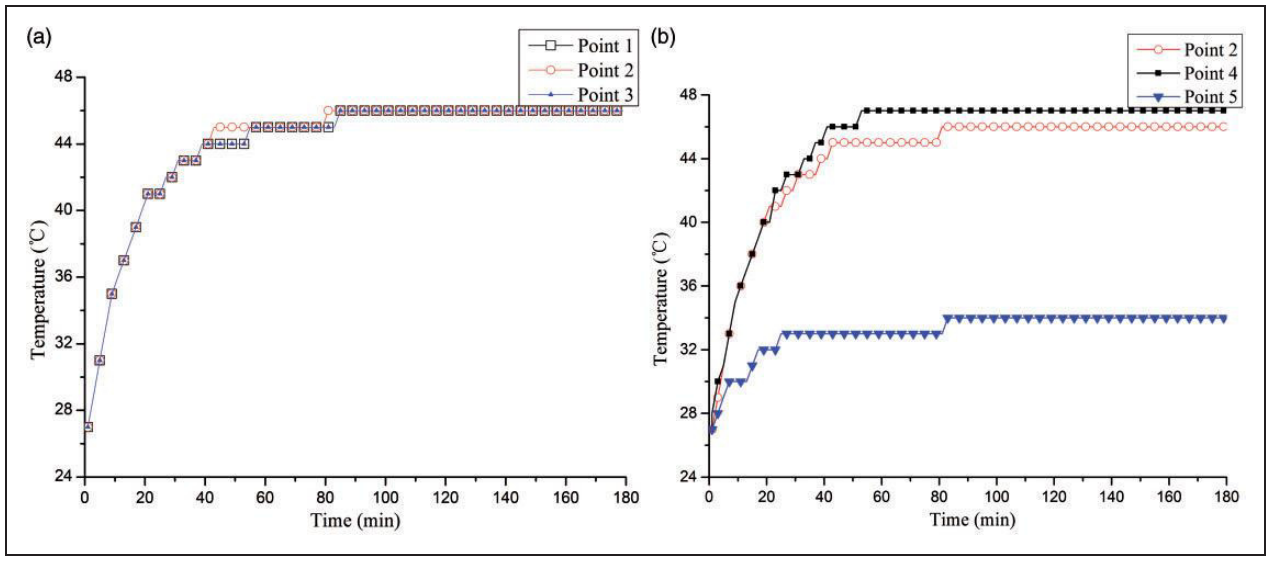

Figure 8. Temperature rise curve of the motorized spindle: (a) the middle section and (b) the front, middle and rear temperature rise curve of the motorized spindle.

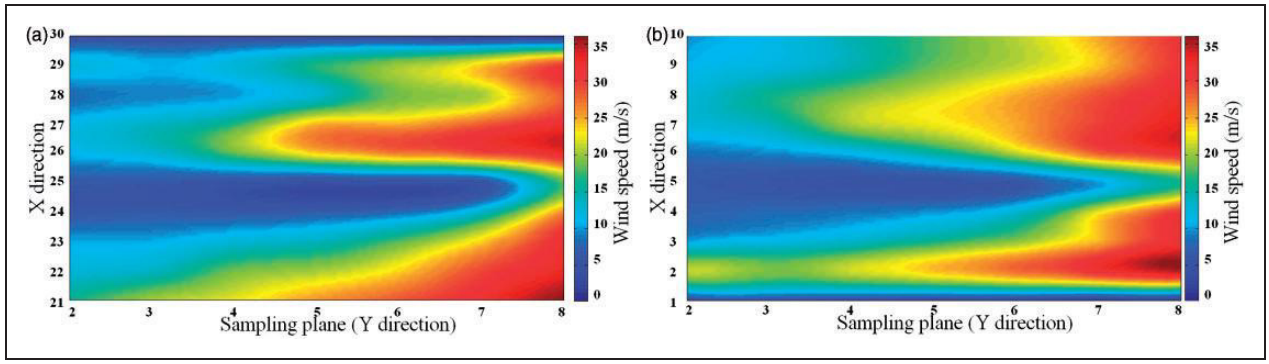

Figure 9. The wind speed in the heat sink grooves: (a) wind speed on the surface A; (b) wind speed on the surface B.

so the ambient temperature is higher. The temperature of the entire motorized spindle increased fast and entered the steady thermal state in about 90 min. After that, the steady-state thermal data of the spindle are recorded.

Wind speed characteristics in the heat sink grooves. The wind speed in all heat sink grooves is shown in Figure 9. The wind speed is reduced in the vents, while for each vent the wind speed is higher in the middle groove than others. The grooves $x = 5$ and $x = 25$ are at the joint of the vents, so the wind speed in those grooves is lower. The grooves $x = 2$ and $x = 29$ are blocked at the ends, which is why the wind speed increases (see the color of the sampling planes 2 and 3). In addition, the results show that the change of the heat sink cross-section area has little effect on the wind speed.

The relationships between the rotating speed, wind speed, surface temperature and noise. The wind speed change in groove $x = 27$ is typical, thus this groove is chosen to represent the wind speed change at different rotating speed. It can be seen from the Figure 10 that the wind speed increases with the rotating speed, and the front, middle and rear wind speed difference is also increasing with it. This illustrates that the kinetic energy dissipation of the fluid is larger when the wind speed is high.

In the temperature rise experiments, the temperature trend of a sampling plane differs only slightly, thus the temperature of the motorized spindle can also be represented by the front, middle and rear points (points 4, 2, 5). Figure 11 shows the temperature of the key points on the motorized spindle. The temperature increases with the rotating speed, although the wind speed also increases. The temperature of the front port is higher than the other parts because it is heated by the bearings and the motor. The temperature of the middle part also increases with the rotating speed, since the heat transmitted to the rear part increased its temperature.

The relationships curves of the rotating speed, vibration and noise are shown in Figures 12 and 13.

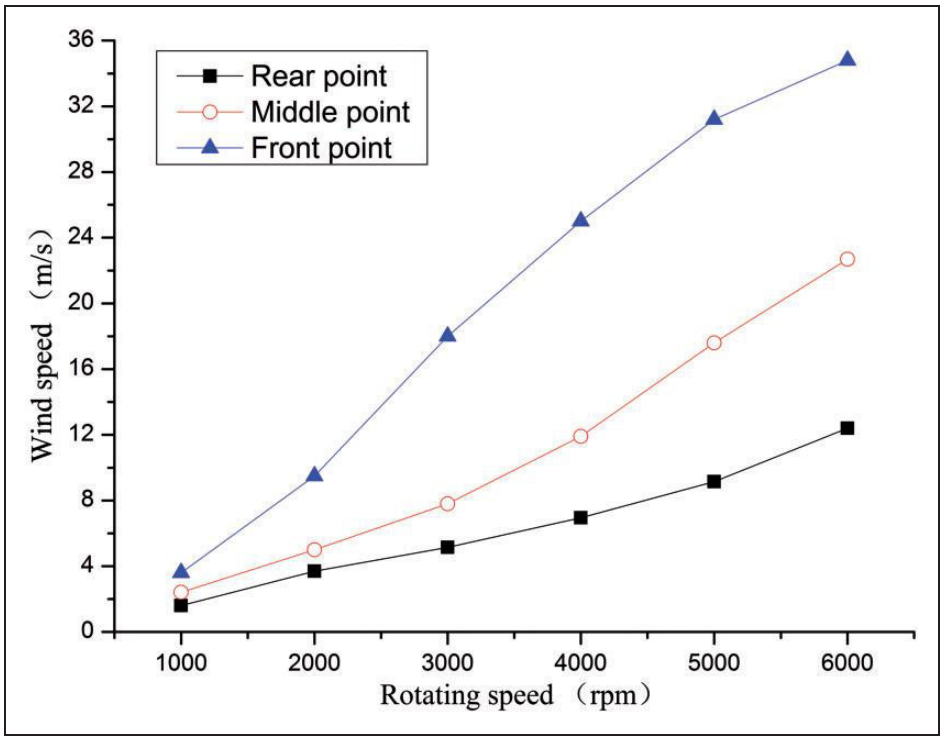

Figure 10. The wind speed and rotating speed curves of the x = 27 groove.

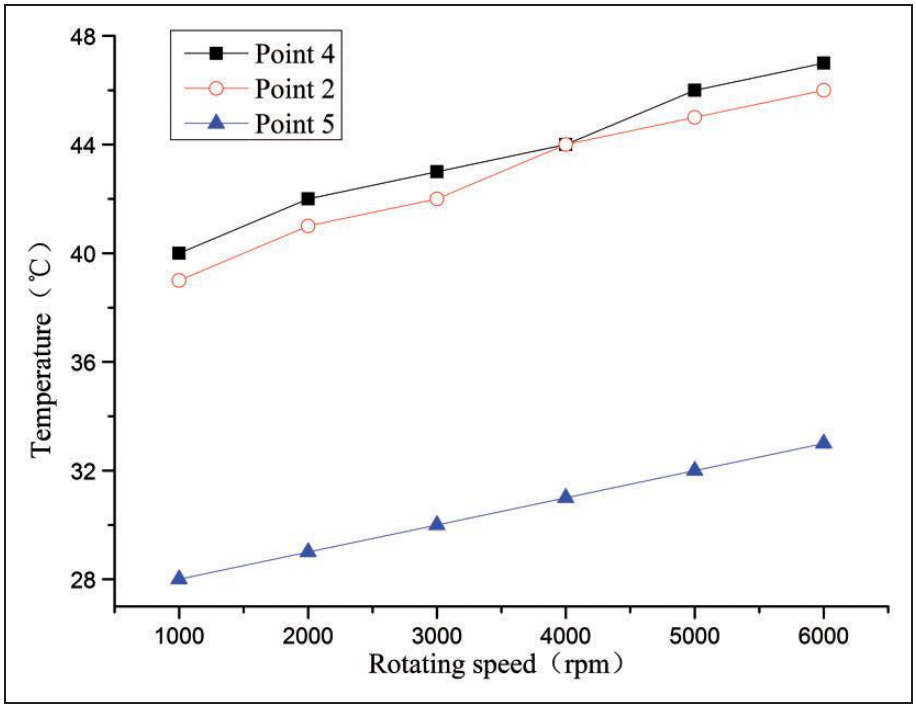

Figure 11. The rotating speed and the temperature curves.

The noise and vibration of the motorized spindle increase with the rotating speed. The noise reaches 103 dB at 4000 r/min and after that the increase of rotating speed only causes a very small noise increase. The vibrations at 3000–4000 r/min rise more slowly than at other rotating speeds.

Comparison of numerical and experimental results

Figure 14 shows the numerical and experimental results of the x = 27 groove, and the results are basically consistent.

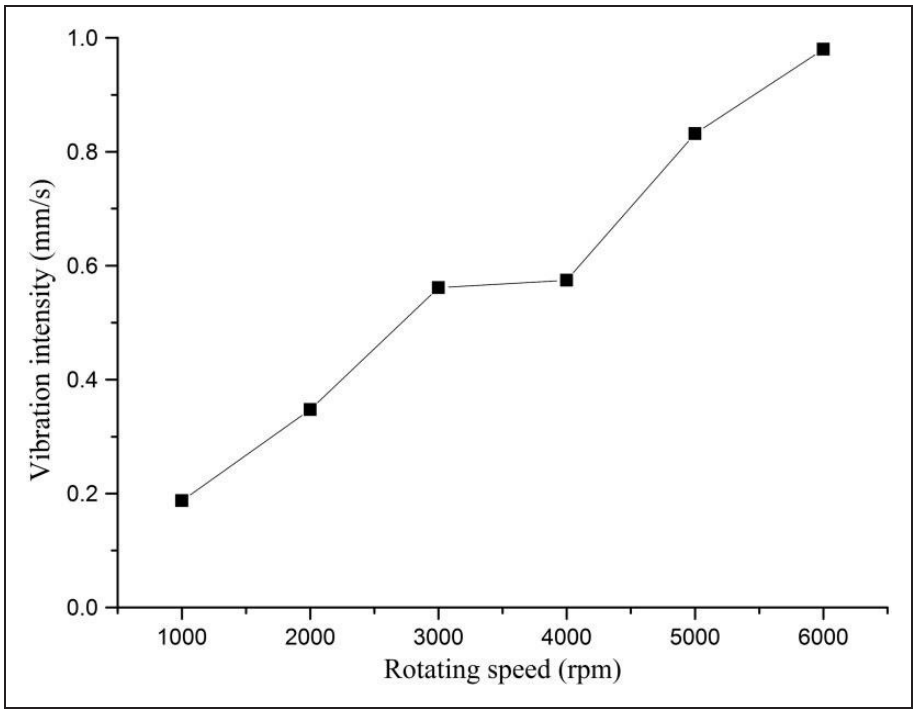

Figure 12. The rotating speed and vibration curve.

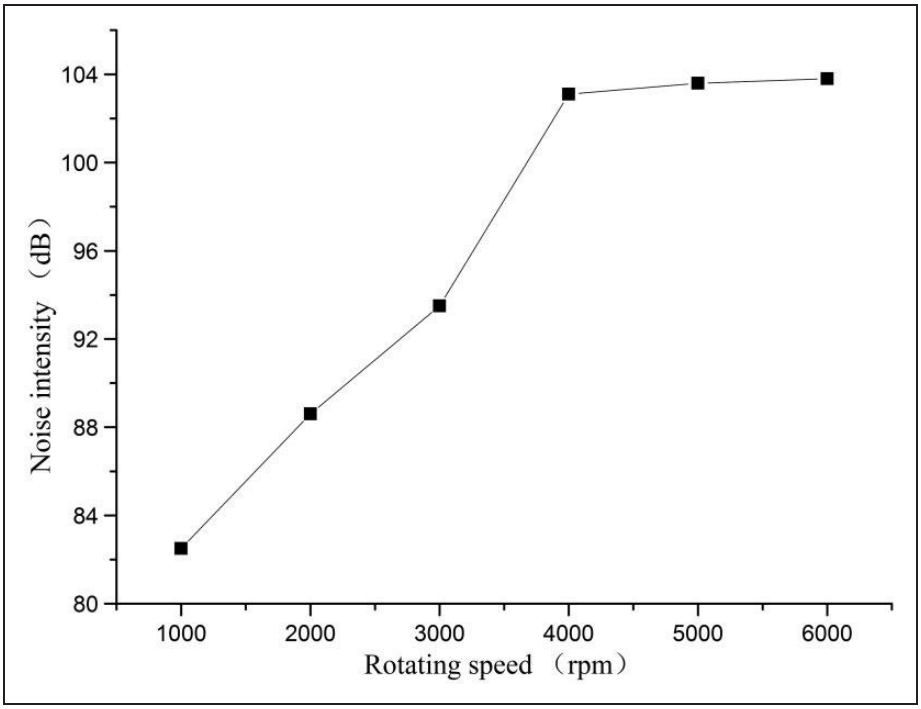

Figure 13. The rotating speed and noise curve.

It is shown in Figure 15 that the maximum temperature areas are in the middle part and the area below the middle part. The reason is that the heat dissipation is not so good in those areas (the cool air is blocked by the joint of the vents in the middle part and by the rear cover in the lower part), and these areas are also close to the stator. The lower-left corner of the surface C is connected with the experimental table, thus this area is cooled, since the heat of the spindle is transmitted to the experimental table. The numerical result of the temperature simulation method is a little higher than the experiment result at the end of the motorized spindle, because the whole heat sink uses the averaged heat transfer coefficient. Figure 16 shows the temperature comparison of the experimental and numerical results in the $x = 15$

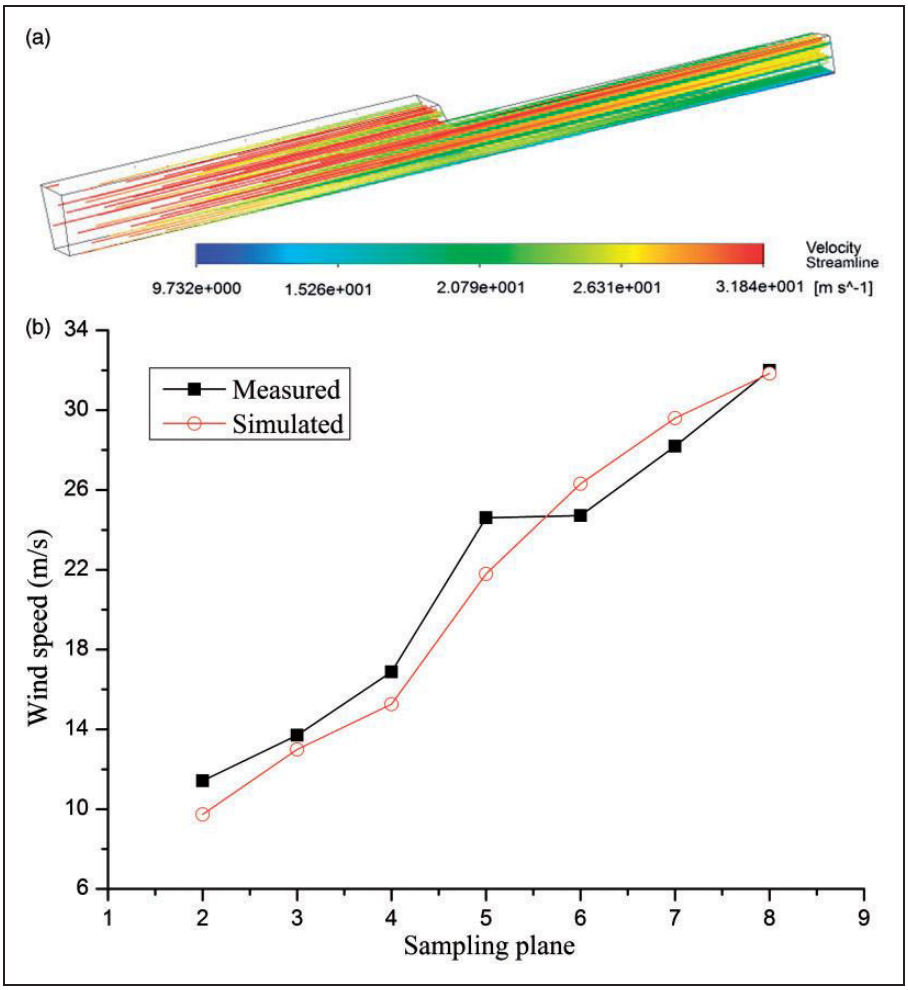

Figure 14. Numerical and experimental results of the x = 27 groove heat sink: (a) numerical results and (b) comparison of the experimental and numerical results.

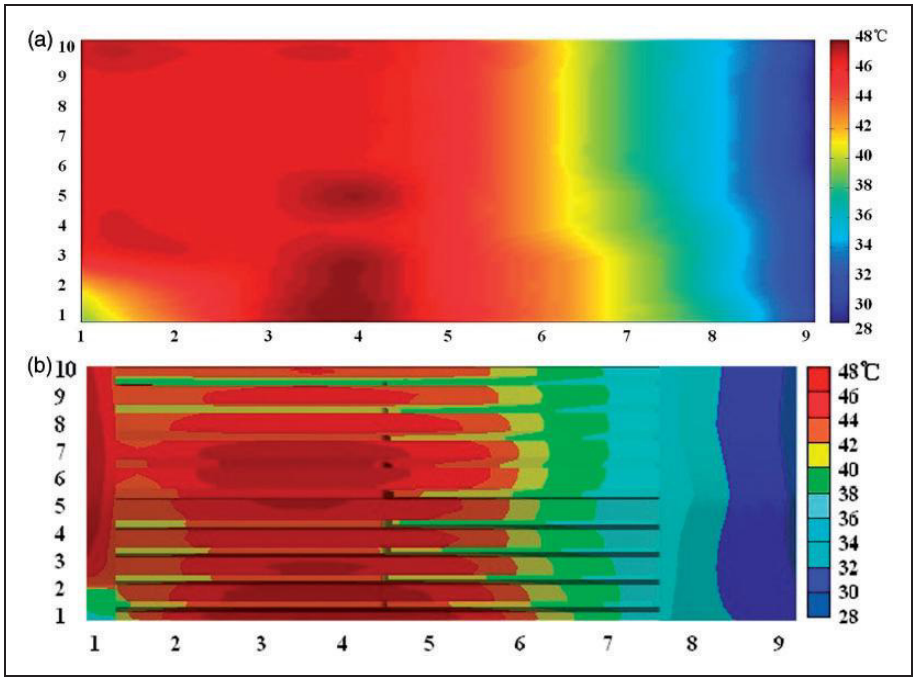

Figure 15. Comparison of the temperature on the surface C: (a) experimental results and (b) numerical results.

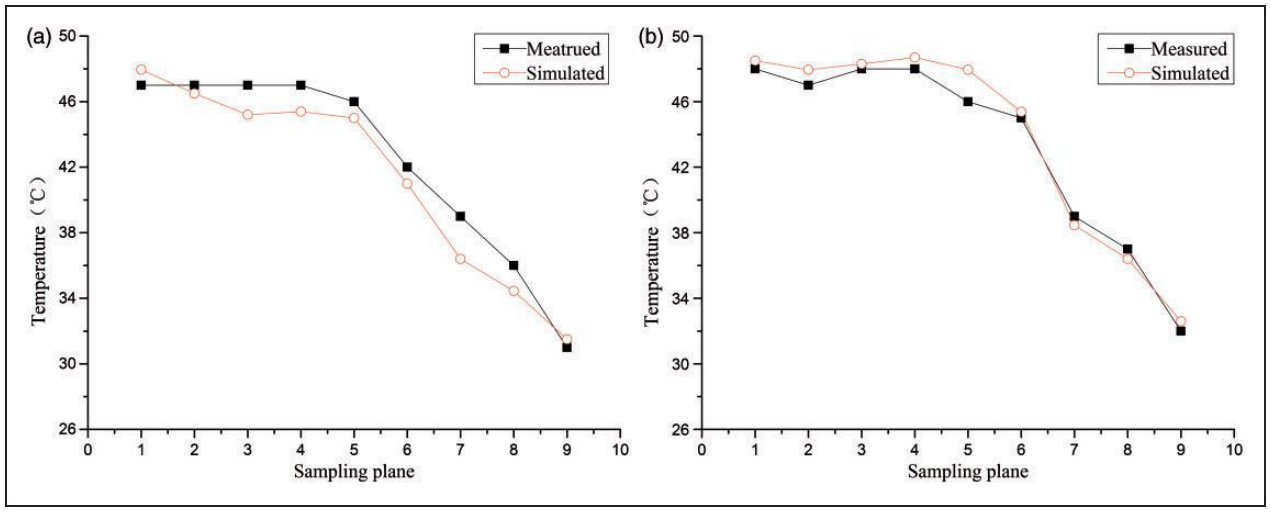

Figure 16. Comparison of the numerical and experimental results: (a) temperature of the x = 15 groove; (b) temperature of the x = 25 groove.

and x = 25 grooves. The temperature distribution of the motorized spindle can be divided into the latter part temperature rise area and the front part stable temperature area, according to Figures 15 and 16. In the latter part rise area, the temperature increases fast and in the front part stable area the temperature is around $47 \pm 1.5^{\circ}C$.

Conclusions

In this paper, numerical model has been developed to simulate the flow and temperature fields of the air-cooled motorized spindle. The temperature rise and the wind speed were studied experimentally. The relationship between the rotating speed, vibration and noise were also investigated by experiments. Numerical and experimental results are comparable.

The numerical result shows that there is a vortex in the upper-left corner of the fan area, the wind speed is higher in the center and lower corner close to the wall. The spindle temperature of areas in contact with the front bearings and the rotor is higher than the other areas. It is shown in the experiments that the temperature of the motorized spindle increases fast in the first 40 min and then reaches the steady thermal state. The wind speed of an operating motorized spindle is higher in the middle groove than other grooves. The change of the heat sink cross-section area has little effect on the wind speed and the kinetic energy dissipation of the fluid is larger when the wind speed is high. The temperature, vibration and noise of the motorized spindle increase with the rotating speed. The temperature is high in the front part and low in the latter part, and the noise has a modest increase past 103 dB. The numerical and experimental results are basically consistent, and show that the temperature variation of the front part is small, while the temperature variation of the latter part is large.

It is suggested to improve the design of the motorized spindle and optimize the blade structure in order to decrease the temperature rise, vibration and noise. Better numerical results can be obtained by using the coupled calculation of the thermal and fluid flow models.

Declaration of Conflicting Interests

The author(s) declared no potential conflicts of interest with respect to the research, authorship, and/or publication of this article.

Funding

The author(s) disclosed receipt of the following financial support for the research, authorship, and/or publication of this article: The project was supported by the National Natural Science Foundation of China (51105002), the National Science and Technology Major Project (2012ZX04005-021), the Natural Science Foundation of the Henan Province (152102210196), and the Foundation of the Henan Educational Committee (16A46001).

References

1. Krulewich DA. Temperature integration model and measurement point selection for thermally induced machine tool errors. *Mechantronics* 1998; 8: 395–412.
2. Sarraf C, Nouri H, Ravelet F, et al. Experimental study of blade thickness effects on the overall and local performances of a controlled vortex designed axial-flow fan. *Exp Therm Fluid Sci* 2011; 35: 684–693.
3. Hurault J, Kouidri S and Bakir F. Experimental investigations on the wall pressure measurement on the blade of axial flow fans. *Exp Therm Fluid Sci* 2012; 40: 29–37.
4. Gomes RPF, Henriques JCC, Gato LMC, et al. Multipoint aerodynamic optimization of the rotor blade sections of an axial-flow impulse air turbine for wave energy conversion. *Energy* 2012; 45: 570–580.
5. Mori M, Novak L and Sekavčnik M. Measurements on rotating blades using IR thermography. *Exp Therm Fluid Sci* 2007; 32: 387–396.

6. Sadowski T and Golewski P. Multidisciplinary analysis of the operational temperature increase of turbine blades in combustion engines by application of the ceramic thermal barrier coatings (TBC). *Comput Mater Sci* 2011; 50: 1326–1335.
7. Fike M, Bombek G, Hriberšek M, et al. Visualization of rotating stall in an axial flow fan. *Exp Therm Fluid Sci* 2014; 53: 269–276.
8. Allison JM, Staats WL, McCarthy M, et al. Enhancement of convective heat transfer in an air-cooled heat exchanger using interdigitated impeller blades. *Int J Heat Mass Transf* 2011; 54: 4549–4559.
9. Zhao H, Yang J and Shen J. Simulation of thermal behavior of a CNC machine tool spindle. *Int J Mach Tools Manuf* 2007; 47: 1003–1010.
10. Holkup T, Cao H, Kolář P, et al. Thermo-mechanical model of spindles. *CIRP Ann Manuf Technol* 2010; 59: 365–368.
11. Anandan KP and Ozdoganlar OB. Analysis of error motions of ultra-high-speed (UHS) micromachining spindle. *Int J Mach Tool Manuf* 2013; 70: 1–14.
12. Zahedi A and Movahhedy MR. Thermo-mechanical modeling of high speed spindles. *Sci Irancia B* 2012; 19: 282–293.
13. Lewis RW, Nithiarasu P and Seetharamu KN. *Fundamentals of the finite element method for heat and fluid flow*. Hoboken, NJ, USA: John Wiley & Sons Inc, 2004.
14. Launder BE and Spalding DB. *Lectures in mathematical models of turbulence*. London, England: Academic Press, 1972.
15. Palmgren A. *Ball and roller bearing engineering*. 3rd ed. Philadelphia: Burbank, 1959, pp.34–41.
16. Harris TA and Kotzalas MN. *Rolling bearing analysis*. 5th ed. Florida: CRC Press, 2006.
17. Gieras J and Wing M. *Permanent magnet motor technology*. 2nd ed. New York: Marcel Dekker, 2002.
18. Rohsenow WM, Hartnett JP and Cho Y. *Handbook of heat transfer*. 3rd ed. New York: McGraw-Hill Professional, 1975, Sec. 6–8.
19. Bao-min W, Chi-bing H, Jian-ren S, et al. Simulation analysis of thermal characteristics of high-speed motorized spindle by using ANSYS. *J Lanzhou Univ Technol* 2009; 35: 1673–5196.
20. Chen Y and Chen Z. *Fundamental theory of machine tool thermal character*. Beijing: China Machine Press, 1989.

Appendix

Notation

A	cross-section area (m^2)
B	magnetic flux (T)
d	characteristic length of the flow pass diameter (m)
f	frequency of the motor (Hz)
f_1	load coefficient (−)
G_b	turbulent kinetic energy generated by buoyancy (−)
G_k	turbulent kinetic energy generated by the average velocity gradient (−)
h_g	heat transfer coefficients of the air gap between rotor and stator ($W/(m^{2\circ}C)$)
h_t	heat transfer coefficients of the spindle surface ($W/(m^{2\circ}C)$)
h_w	heat transfer coefficients of the heat sink ($W/(m^{2\circ}C)$)
I_p	phase current of the rotor winding or stator (A)
k	turbulent kinetic energy, (m^2s^{-2})
L_p	length of each phase winding (m)
M	friction torque ($N?mm$)
M_1, M_2	friction torque ($N\ mm$)
n	rotating speed of the bearing inner race (r/min)
Nu, Nu_f	Nusselt number (−)
P_1	equivalent load of the bearings (N)
$P_{1/50}$	iron loss coefficient when $B = 1\ T$ and $f = 50$ (−)
P_{cm}	copper loss (W)
P_{Fe}	iron loss (W)
Pr_f	Prandlt number
Pr_w	temperature coefficient (°C)
R	characteristic length (m)
Re	Reynolds number (−)
r	resistance of single-phase rotor winding or stator winding (Ω)
S	cross-sectional area of the conductor (m^2)
t	time, (s)
T	temperature, (K)
T_f	average value of fluid temperature (°C)
T_w	wall temperature (°C)
u_i	the average inlet velocity in the i direction (−)
$\bar{v}$	mean flow velocity of the fluid (m/s)
x	wetted perimeter of the cross-section (m)
x_i	xi direction (−)
Y_M	influence of compressible turbulent flow pulsation on total dissipation rate (−)
α	thermal diffusivity (−)
ε	dissipation rate of turbulent kinetic energy, (m^2s^{-3})
θ	phase number of the motor (−)
λ_w	thermal conductivity of the fluid ($W/(m^{\circ}C)$)
μ_i	turbulent viscosity coefficient (−)
ν	kinematic viscosity of the fluid (m^2/s)
ρ	density of the fluid ($kg?m^{-3}$)
ρ_p	resistivity of the winding ($_{\Omega}{\cdot}m$)
Φ	entire heat transfer (−)
Φ_c	convection heat transfer (−)
Φ_R	radiation heat transfer (−)